EUROPEAN JOURNAL OF PURE AND APPLIED MATHEMATICS
2026, Vol. 19, Issue 3, Article Number 7934
ISSN 1307-5543 – ejpam.com
Published by New York Business Global

Numerical Analysis of Cattaneo–Christov Heat and Mass Flux Effects on MHD Radiative Casson–Jeffrey Fluid Flow over a Riga Plate with Double Stratification

Khulud Ziadi*

[1] *Mathematics Department, Faculty of Sciences, Umm Al-Qura University, Makkah, Saudi Arabia*

Abstract. This work emphases on the comparative analysis of Casson-Jeffrey fluid on heat and mass transfer in MHD radiative flow over the Riga Plate, considering Cattaneo-Christov heat and mass fluxes, chemical reactions, cross-diffusion, dual stratification, thermophoresis, Brownian motion, and free convection impact fluid behaviour. The Riga sheet is used to estimate the characteristics of both laminar and turbulent fluid flows. This problem is highly important, as these factors play a crucial role in shaping engineering procedures and applications that involve non-Newtonian liquids. The symmetry concept is employed to identify appropriate similarity transformations and reduce the governing nonlinear partial differential equations (PDEs) into a system of ordinary differential equations (ODEs), which are later computed numerically through the bvp4c solver with MATLAB. The findings of this study indicate that as G_T increases from 0.1 to 1.3, the skin-friction coefficient changes by 23.20% for the Casson fluid and 34.00% for the Jeffrey fluid. As the radiation parameter increases from 0.2 to 0.8, the heat-transfer rate increases by approximately 13.73% for the Casson fluid and 4.57% for the Jeffrey fluid. Furthermore, increasing the Soret number and thermophoresis parameters increases the concentration, while chemical reactions have the opposite effect. The novelty of this study is that Jeffery fluid exhibits lower velocities and higher temperatures than Casson fluid. However, the concentration remains largely the same during diffusion, resulting in a nearly identical profile.

2020 Mathematics Subject Classifications: 76W05, 76A05, 76M25, 80A20, 80A22, 35Q35
Key Words and Phrases: Riga plate, Casson-Jeffrey fluid, Cattaneo-Christov heat-mass flux, double stratification, thermophoresis, Brownian motion

1. Introduction

A magneto-hydrodynamic phenomenon known as fluid flow in a Riga plate occurs when an electrically conducting fluid passes over a certain surface made up of alternating electrodes and magnets. By precisely controlling the fluid boundary layer, this configuration produces a Lorentz force that lowers resistance and boosts heat transfer. This

*Corresponding Author.
DOI: https://doi.org/10.29020/nybg.ejpam.v19i3.7934

Email address: ksziadi@uqu.edu.sa (K. Ziadi)

 Copyright: © 2026 The Author(s). (CC BY-NC 4.0)

makes it useful for applications where flow modification is essential, like aerodynamics, heat exchangers, and micro-coolers. The hydrodynamic behavior of a Maxwell liquid on a Riga plate was thoroughly examined by Alrihieli et al. [1]. Alwawi et al. [2] explored how an unsteady micropolar nanofluid behaves when moving over a vertically positioned Riga sheet that stretches nonlinearly. The Darcy–Forchheimer nanofluid passing through a Riga plate was investigated by Ali et al. [3]. Alhazmi et al. [4] examined the role of chemical reactions in non-Newtonian convective flow over a Riga plate. Ahmed et al. [5] used the Casson model to study 3D incompressible hybrid nanofluid flow on a smooth Riga surface. Ajala et al. [6] explored the effects of solar radiation and variable thermophysical properties on Casson liquid with magnetic ground. Ali et al. [7] evaluated nanoparticle flow generated by a Williamson fluid over a Riga plate. A continuous, 2-D Casson hybrid nanofluid flow in a converging/diverging channel was scrutinized by Bhaskar et al. [8]. Bhaskar et al. [9] inspected the vertical microchannel stream of two immiscible non-Newtonian fluids designated by the Jeffrey and Casson models. The effects of changing fluid characteristics on magnetohydrodynamic incompressible Maxwell nanofluids were examined by Basha et al. [10]. Choudhary et al. [11] investigated the behaviour of bio convective MHD Casson mixed nanoliquid. Choudhary et al. [12] scrutinized the impression of a moving thin needle on a magnetohydrodynamic chemically reactive Williamson mix nanoliquid. Choudhary et al. [13] examined the influences of radiation on the Casson flow of hybrid nanofluid across a moving plate. Eswaramoorthi et al. [14] examined the flow of Sutterby nanoliquid in porous media while taking inertial and viscous factors into consideration. Galal et al. [15] looked at how radiation affected the ternary hybrid nanofluid on a Riga plate. The temperature and mass diffusion characteristics of chemically reactive and magnetite hybrid nanofluids flowing across a Riga plate were investigated by Govind et al. [16]. Mehmood et al. [17] investigated the magnetohydrodynamic flow of a hybrid nanofluid past an angled Riga plate. The combined effects on Carreau ternary hybrid nanofluid flow through a vertical stretching cylinder are considered through Mehta et al. [18]. The effects of Newtonian liquid movement on an electromagnetic (Riga) surface experiencing cross-diffusion and Brownian motion were examined by Muhammad et al. [19]. The effects of viscous dissipation and entropy generation on Maxwell nanofluid flow were investigated by Sachin et al. [20]. Shankar et al. [21] calculated nanoliquid flow with double-diffusion effects over both a wedge and a cone. The intricate subtleties of heat transport in magnetohydrodynamic schemes, including fluid behavior, were examined by Thenmozhi et al. [22]. The convective heat and mass transfer properties of non-Newtonian liquids flowing up a vertical cone were thoroughly investigated by Varshegaa et al. [23]. Yasmin et al. [24] studied the formation of magnetohydrodynamic irreversibility produced by the moving Riga plate in weakly conducting dissipative Casson fluid flow. The properties of magnetohydrodynamic Williamson nanofluid flow past a nonlinear stretching surface were investigated by Kumar et al. [25]. Magnetohydrodynamics Casson hybrid nanofluid flow across a stretched surface was introduced by Ramasekhar et al. [26]. The constant two-dimensional bioconvective flow of a Casson fluid across a thin needle was investigated by Iranian et al. [27]. The primary objective of this analysis is to discuss a comparative investigation of MHD steady Casson-Jeffrey liquid flow on the Riga Plate,

including the impacts of Cattaneo-Christov heat-mass flux, free convection, and dual diffusion. Previous studies have not yet tried to explain this precise feature of the essential interaction between Casson and Jeffrey fluids, including double stratification. The novelty of this study is described as follows

- This research offers an in-depth investigation of fluid behavior by evaluating two distinct non-Newtonian models (Jeffrey and Casson fluids) while incorporating the effects of thermal radiation, cross-diffusion, buoyancy ratio, Cattaneo–Christov heat and mass flux, thermophoresis, and Brownian motion. By integrating these factors, the study enhances the understanding of complex transport processes and yields valuable insights applicable to improving efficiency in industrial operations, environmental systems, and biomedical technologies.
- The Riga plate, which generates electromagnetic forces, brings Lorentz forces into the flow system. These forces strongly influence both fluid motion and heat transfer.
- By analyzing the interaction between magnetic fields and fluid transport in porous structures, this study provides insights applicable to devices and processes including electromagnetic pumps, thermal exchangers, and petroleum recovery operations.
- The incorporation of chemical reactions captures the role of reactive species, broadening the model's potential applications in catalytic and biochemical processes.

2. Mathematical Formulation

Consider the steady MHD double diffusive Casson-Jeffrey fluid flow with the modified Buongiorno model over a permeable Riga plate in the existence of free convection and Cattaneo-Christov heat-mass flux. In Figure 1, assume that the x-axis is on the surface and the y-axis is perpendicular to the Riga plate. The Riga plate should be preserved at a constant thermal $T_w$and solute level C_w.

The boundary-layer flow behavior can be described by the governing equations presented below, following the Refs. [4], [9], and [21].

Eq. of continuity

$$\frac{\partial u}{\partial x}+\frac{\partial v}{\partial y}=0. \tag{1}$$

Equation of motion:

$$\begin{aligned} u\frac{\partial u}{\partial x}+v\frac{\partial u}{\partial y}=\vartheta\left(1+\frac{1}{\beta}\right)\frac{\partial^2 u}{\partial y^2}+K_0\left(u\frac{\partial^3 u}{\partial x\partial y^2}+\frac{\partial u}{\partial x}\frac{\partial^2 u}{\partial y^2}\right.\\ \left.+\frac{\partial u}{\partial y}\frac{\partial^2 v}{\partial y^2}+v\frac{\partial^3 u}{\partial y^3}\right)+\frac{\pi J_0 M_0}{8\rho}\exp\left(-\frac{\pi}{a_1}y\right)+g\beta_T(T-T_\infty)-\frac{u}{k}\vartheta. \end{aligned} \tag{2}$$

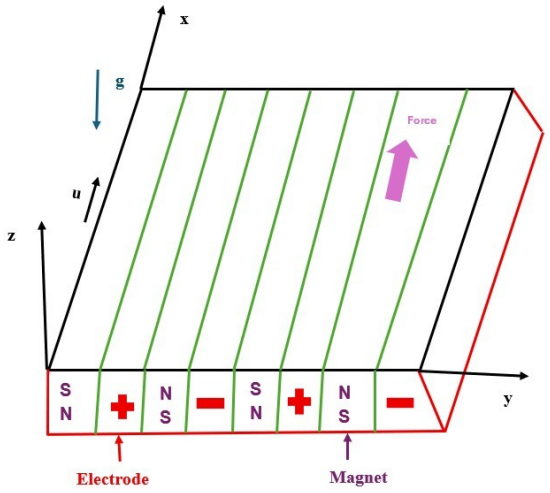

Figure 1: Fluid flow over a Riga plate

Equation of temperature:

$$u\frac{\partial T}{\partial x}+v\frac{\partial T}{\partial y}=\alpha\left(1+\frac{16\sigma^{*}T_{\infty}^{3}}{3kk^{*}}\right)\frac{\partial^{2}T}{\partial y^{2}} - \lambda_{T}\left(u\frac{\partial T}{\partial x}\frac{\partial u}{\partial x}+v\frac{\partial T}{\partial y}\frac{\partial v}{\partial y}+u^{2}\frac{\partial^{2}T}{\partial x^{2}}+v^{2}\frac{\partial^{2}T}{\partial y^{2}}+2uv\frac{\partial^{2}T}{\partial x\partial y}+u\frac{\partial T}{\partial y}\frac{\partial v}{\partial x}+v\frac{\partial T}{\partial x}\frac{\partial u}{\partial y}\right) + \frac{Q_{0}}{\rho C_{p}}\left(T-T_{\infty}\right)+\tau\left(D_{B}\frac{\partial T}{\partial y}\frac{\partial C}{\partial y}+\frac{D_{T}}{T_{\infty}}\left(\frac{\partial T}{\partial y}\right)^{2}\right)+\frac{D_{m}K_{T}}{C_{p}C_{s}}\frac{\partial^{2}C}{\partial y^{2}}. \tag{3}$$

Equation of concentration:

$$u\frac{\partial C}{\partial x}+v\frac{\partial C}{\partial y}=D_{B}\frac{\partial^{2}C}{\partial y^{2}} - \lambda_{C}\left(u\frac{\partial C}{\partial x}\frac{\partial u}{\partial x}+v\frac{\partial C}{\partial y}\frac{\partial v}{\partial y}+u^{2}\frac{\partial^{2}C}{\partial x^{2}}+v^{2}\frac{\partial^{2}C}{\partial y^{2}}+2uv\frac{\partial^{2}C}{\partial x\partial y}+u\frac{\partial C}{\partial y}\frac{\partial v}{\partial x}+v\frac{\partial C}{\partial x}\frac{\partial u}{\partial y}\right) - k_{1}\left(C-C_{\infty}\right)+\frac{D_{T}}{T_{\infty}}\frac{\partial^{2}T}{\partial y^{2}}+\frac{D_{m}K_{T}}{T_{m}}\frac{\partial^{2}T}{\partial y^{2}}. \tag{4}$$

The additions applied in this study use ref. [4].

$$\begin{aligned} &u = U_w + \lambda\frac{\partial u}{\partial y}, \quad v = V_w, \quad T = T_w = T_0 + bx, \quad C = C_w = C_0 + cx, \qquad \text{at } y = 0, \\ &u = 0, \quad \frac{\partial u}{\partial y} \to 0, \quad T \to T_\infty = T_0 + dx, \quad C \to C_\infty = C_0 + ex, \qquad \text{as } y \to \infty. \end{aligned} \tag{5}$$

The similarity transformations:

$$\begin{aligned} u = axf'(\eta), \qquad v = -\sqrt{a\nu}\, f(\eta), \\ \theta(\eta) = \frac{T - T_\infty}{T_w - T_0}, \qquad \phi(\eta) = \frac{C - C_\infty}{C_w - C_0}, \qquad \eta = y\sqrt{\frac{a}{\nu}}. \end{aligned} \tag{6}$$

Substituting Equation 6 into Equations 2-5 and rearranging them yields the updated differential equation:

$$\left(1 + \frac{1}{\beta}\right) f''' + ff'' + K\left(2f'f''' - ff'''' - f''^2\right) - f'^2 + Hm\, e^{-\beta_1\eta} + G_T\theta - K_1 f' = 0. \tag{7}$$

$$\begin{aligned} \frac{1}{Pr}(1 + Nr)\,\theta'' + f\theta' - f'\theta - S_1 f' + Q\theta + Nb\,\theta'\phi' + Nt\,\theta'^2 + Du\,\phi'' \\ -\gamma_T\Big(f'^2\theta + S_1 f'' - ff'\theta' - ff''\theta - S_1 ff'' + f^2\theta''\Big) = 0. \end{aligned} \tag{8}$$

$$\begin{aligned} \phi'' + Sc\, f\phi' - Sc\, f'\phi - S_2 Sc\, f' - Kr\, Sc\,\phi \\ -Sc\,\gamma_C\Big(f'^2\phi + S_2 f'^2 - ff'\phi' - ff''\phi - S_2 ff'' + f^2\phi''\Big) \\ +Sc\, Sr\,\theta'' + \frac{Nt}{Nb}\theta'' = 0. \end{aligned} \tag{9}$$

subject to the boundary conditions

$$\begin{aligned} &f(0) = f_w, \qquad f'(0) = 1 + \delta f''(0), \qquad \theta(0) = 1 - S_1, \qquad \phi(0) = 1 - S_2, \qquad \text{at } \eta = 0, \\ &f'(\infty) \to 0, \qquad \theta(\infty) \to 0, \qquad \phi(\infty) \to 0, \qquad \text{as } \eta \to \infty. \end{aligned} \tag{10}$$

When $\frac{1}{\beta} \to 0$ and $K \neq 0$, then fluid behaves like Jeffrey fluid, and when $K = 0$ and $\frac{1}{\beta} \neq 0$, then the fluid behaves like Casson fluid.

Here, Casson fluid parameter (β), Jeffrey fluid parameter (K), Hartmann number, (Hm), porous media (K_1), Prandtl number (Pr), thermal, and solute relaxation coefficients (γ_T, γ_c), Grashof number(G_T), radiation parameter (Nr), chemical reaction (Kr), heat source (Q), thermophoresis (Nt), Brownian motion (Nb), Dufour effect (Du), Soret effect (Sr), Suction/injection parameter (f_w), velocity slip parameter (δ), thermal and mass stratification parameter (S_1, S_2)and Schmidt number (Sc). The variables are arranged numerically as follows:

$$Hm = \frac{\pi j_0 M_0}{8U_w \rho a}, \qquad Pr = \frac{\nu}{\alpha}, \qquad G_T = \frac{g(T_w - T_0)\beta_T}{xa^2},$$

$$Sr = \frac{D_m K_T (T_w - T_0)}{T_m \nu (C_w - C_0)}, \qquad Du = \frac{D_m K_T (C_w - C_0)}{C_s C_p (T_w - T_0)\nu},$$

$$f_w = \frac{v_w}{\sqrt{a\nu}}, \qquad Q = \frac{Q_0}{\rho a C_p}, \qquad Nr = \frac{16\sigma T_\infty^3}{3kk^*},$$

$$K = \frac{K_0}{a}, \qquad \gamma_T = \lambda_T a, \qquad \gamma_C = \lambda_C a,$$

$$\delta = \lambda\sqrt{\frac{a}{\nu}}, \qquad K_1 = \frac{\nu}{ka}, \qquad Sc = \frac{\nu}{D_B},$$

$$Kr = \frac{k_1}{a}, \qquad Nt = \frac{\tau D_T (T_w - T_0)}{\nu T_\infty}, \qquad Nb = \frac{\tau D_B (C_w - C_0)}{\nu},$$

$$S_1 = \frac{d}{b}, \qquad S_2 = \frac{e}{c}, \qquad \beta_1 = \frac{\pi}{a_1\sqrt{a/\nu}}.$$

Physical Quantities

skin friction coefficient $C_f = \dfrac{2\tau_w}{U_w^2 \rho}$, where τ_w is surface shear stress,

$$\frac{C_f Re^{1/2}}{2} = (1 + 3K)\left(1 + \frac{1}{\beta}\right) f''(0) \tag{11}$$

The Nusselt number $Nu_x = \dfrac{x q_w}{k(T_w - T_\infty)}$, Where $q_w = -k\left(\dfrac{\partial T}{\partial y}\right)_{y=0} + (q_r)_{y=0}$

$$Nu_x Re_x^{-1/2} = -(1 + Nr)\theta'(0) \tag{12}$$

The Sherwood parameter $Sh_x = \dfrac{-x q_m}{D_B(C_w - C_\infty)}$

Where $q_m = -D_B\left(\dfrac{\partial C}{\partial y}\right)_{y=0}$ then

$$Sh_x Re_x^{-1/2} = -\phi'(0) \tag{13}$$

Numerical Structure

The transformed nonlinear ordinary differential equations were solved numerically using the MATLAB bvp4c boundary-value problem solver. The computational domain was discretized using an adaptive mesh, and suitable initial guesses were provided for the dependent variables and their derivatives. The relative and absolute tolerances were set

to 10^{-6} and 10^{-8}, respectively, to ensure numerical accuracy. The solution was considered converged when the maximum residual of the governing equations was within the prescribed tolerance and further mesh refinement produced negligible changes in the dependent variables and engineering quantities, including the skin-friction coefficient, Nusselt number, and Sherwood number. The far-field boundary location was also progressively increased until further extension of the computational domain resulted in negligible changes in the numerical solution. These criteria ensured the stability, accuracy, and reliability of the reported numerical results. Let $f = y(1),\ f' = y(2),\ f'' = y(3),\ f''' = y(4),\ \theta = y(5),\ \theta' = y(6),\ \phi = y(7),\ \phi' = y(8)$

Problems 7 to 10 are transformed into the following updated format.

$$\left(1+\frac{1}{\beta}\right) y(4) + y(1)y(3) + K\left(2y(2)y(4) - y(1)f'''' - y(3)^2\right) - y(2)^2 \\ +Hme^{-\beta_1\eta} + G_T y(5) - K_1 y(2) = 0 \tag{14}$$

$$\frac{1}{Pr}(1+Nr)\theta'' + y(1)y(6) - y(2)y(5) - S_1 y(2) + Qy(5) + Nb\, y(6)y(8) + Nt\, y(6)^2 \\ +Du\,\phi'' - \gamma_T\left(y(2)^2 y(5) + S_1 y(2)^2 - y(1)y(2)y(6) - y(1)y(3)y(5) - S_1 y(1)y(3) + y(1)^2\theta''\right) = 0 \tag{15}$$

$$\phi'' + Sc\, y(1)y(8) - Sc\, y(2)y(7) - S_2 Sc\, y(2) - Kr\, Sc\, y(7) \\ -Sc\,\gamma_C\left(y(2)^2 y(7) + S_2 y(2)^2 - y(1)y(2)y(8) - y(1)y(3)y(7) - S_2 y(1)y(3) + y(1)^2\phi''\right) \\ +Sc\, Sr\,\theta'' + \frac{Nt}{Nb}\theta'' = 0 \tag{16}$$

Together with the boundary conditions under consideration

$$y0(1) = f_w, \qquad y0(2) = 1 + \delta y(3), \qquad y0(5) = 1 - S_1, \qquad y0(7) = 1 - S_2, \qquad \text{at } \eta = 0, \\ y\infty(3) \to 0, \qquad y\infty(5) \to 0, \qquad y\infty(7) \to 0, \qquad \text{at } \eta \to \infty \tag{17}$$

Validation

Comparisons with contemporary research findings were undertaken in order to validate the current results. The observed agreement, which is summed up in Table 1, validates the precision and dependability of the present analysis.

Table 1: Validation of the current findings with Alhazmi et al. [4] and the related strategy.

K	**Alhazmi et al. [4]**	**Present study**
-0.3	0.11957924	0.11957608
-0.2	0.44723894	0.44723821
-0.1	0.73780922	0.737809227
0.0	1.00000892	1.00000843
0.1	1.23959440	1.23959440
0.2	1.46064632	1.46064955
0.3	1.66640124	1.666401291

Results and Discussion

This section investigates the behavior of a non-Newtonian magnetohydrodynamic Casson-Jeffrey fluid flowing over a Riga plate, considering combined effects. This study observes the impacts of various flow parameters, including velocity, thermal, solute, skin friction coefficient, Nusselt number, and mass transfer rate, on the flow behaviour. Here,

$$Hm = 0.1, \quad f_w = 1, \quad Nr = 0.2, \quad Pr = 0.5, \quad G_T = 0.1, \quad S_1 = 0.01, \quad S_2 = 0.01,$$

$$Du = 0.2, \quad Sr = 0.5, \quad Nb = 1, \quad Nt = 0.1, \quad Q = 0.05, \quad \delta = 0.01, \quad Kr = Sc = 0.5,$$

$$\gamma_T = \gamma_C = 0.01, \quad K_1 = 0.3, \quad K = 0.3, \quad \beta = 0.1.$$

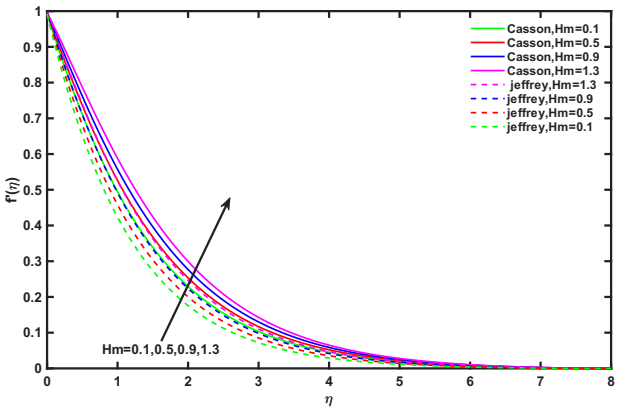

Figure 2: Velocity profile for $0.1 \leq Hm \leq 1.3$.

Figure 2 shows that the velocity profile for both fluids increases as the intensity Hm is increased. In fig.3, when the magnetic constraint rises, the thermal distribution declines for both Casson and Jeffrey fluids owing to the reduction in the width of the thermal boundary layer. Fig.4 shows that when the thermal buoyancy number increases, the velocity gradient intensifies for both Casson and Jeffrey fluids. This is because a larger Grashoff number strengthens the buoyancy force, which reduces the effect of viscous forces, resulting in higher velocities. Casson fluids exhibit slightly higher values than Jeffrey fluids because

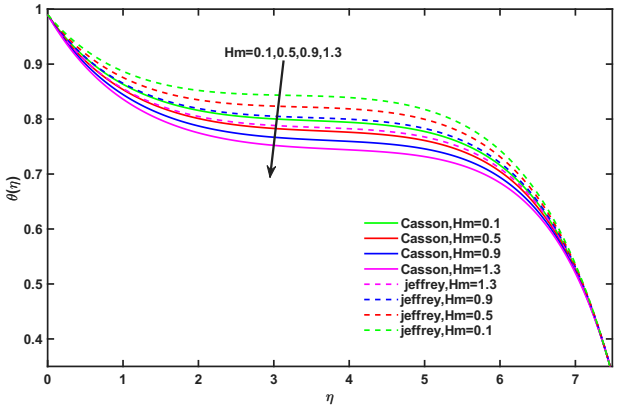

Figure 3: Temperature profile for $0.1 \leq Hm \leq 1.3$.

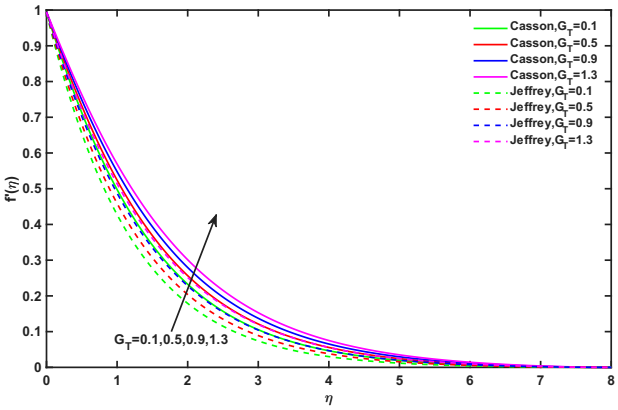

Figure 4: Velocity profile for $0.1 \leq G_T \leq 1.3$

the viscoelastic effects of the Jeffrey model inhibit acceleration more than Casson fluids. Fig. 5 indicates that higher porosity values lead to a reduction in the velocity profile. Larger porosity means a more resistive porous medium, which increases the Darcy drag force and reduces permeability. As a result, the porous matrix absorbs more momentum, slowing the fluid.

In Figure 6, Increasing the Dufour number broadens the thermal outline because the heat transfer from concentration becomes stronger. Jeffery fluid shows higher temperatures than Casson fluid due to its lower effective viscosity and greater heat transport capacity. Figure 7 shows that for $\eta \leq 3.5$, the thermal profile increases because the radiative heat flux near the wall is greater, generating thermal energy. For $\eta > 3.5$, the radiative effect weakens and the heat dissipates, so the temperature gradually decreases and approaches the surrounding value. In Figure 8 illustrates that increasing the Brownian motion parameter enhances the random motion of nanoparticles, thereby intensifying nanoparticle–fluid interactions and energy transport, which results in an increase in the temperature profile. The Jeffery fluid exhibits a higher temperature profile than the Casson fluid, owing to the differences in their rheological characteristics and associated momentum–thermal transport. Furthermore, as shown in Figure 9, the temperature profile increases with the

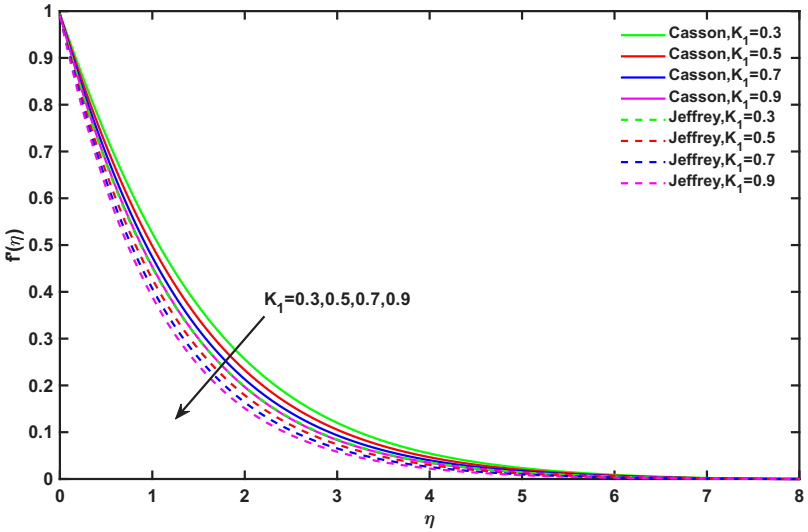

Figure 5: Velocity profile for $0.3 \leq K_1 \leq 0.9$

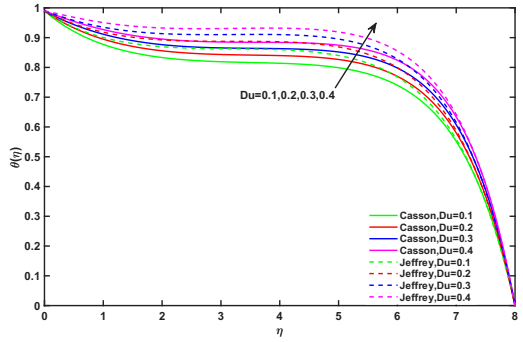

Figure 6: Temperature profile for $0.1 \leq Du \leq 0.4$

thermophoresis parameter. An increase in Nt enhances the thermophoretic migration of nanoparticles along the temperature gradient, thereby modifying the nanoparticle heat transport and contributing to an increase in the fluid temperature. Figure 10 shows that as the Prandtl number increases, for $\eta \leq 4$, the temperature profile decreases because the thermal diffusivity near the wall decreases more and for $\eta > 4$, the temperature profile increases because of the growth in the width of the thermal boundary layer. Figure 11, increasing the heat generation parameter Q rises the amount of thermal energy added to the liquid. Consequently, the temperature profile widens. Jeffrey fluid maintains a higher temperature due to the relaxation effect, while Casson fluid cools faster due to its yield stress behaviour. Figure 12 explains that increasing thermal stratificationS_1 weakens the heat transfer from the surface because the ambient temperature drops rapidly with height. This causes the thermal boundary layer to shrink and the temperature distribution to decline. Figure 13 shows that an increase in the thermal relaxation parameter increases the temperature profile. The larger relaxation time reduces the rate of heat transfer from the fluid, causing greater heat retention and consequently increasing the temperature within

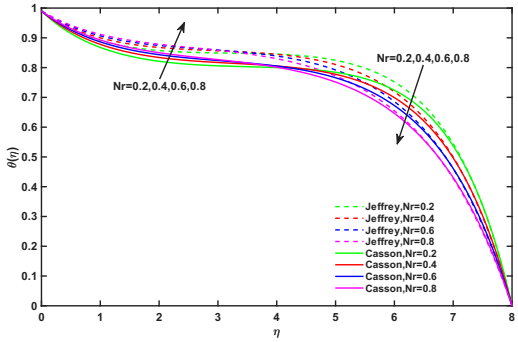

Figure 7: Temperature profile for $0.2 \leq Nr \leq 0.8$

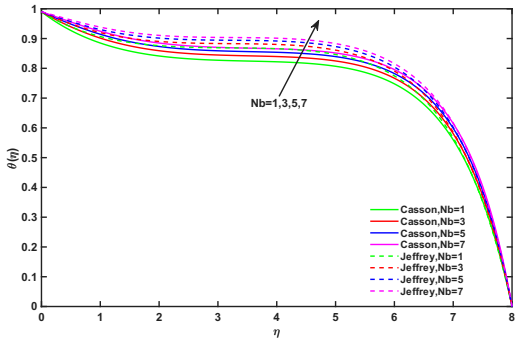

Figure 8: Velocity profile for $0.3 \leq K_1 \leq 0.9$

the boundary layer.

In Figure 14, Increasing the Soret number increases the thermo-diffusion effect, which increases the extra mass flux due to the temperature gradient; this increases the concentration. Jeffrey fluid shows higher concentration than Casson fluid because its viscoelastic nature provides less resistance to deformation. Figure 15 shows that as growing Sc lessens the mass diffusivity, causing the concentration to decrease faster, and Casson fluid shows a lower concentration due to its greater resistance to flow than Jeffrey fluid. Figure 16 shows that increasing the Brownian motion parameter decreases the nanoparticle concentration profile. Higher Nb enhances the random motion and diffusion of nanoparticles, causing

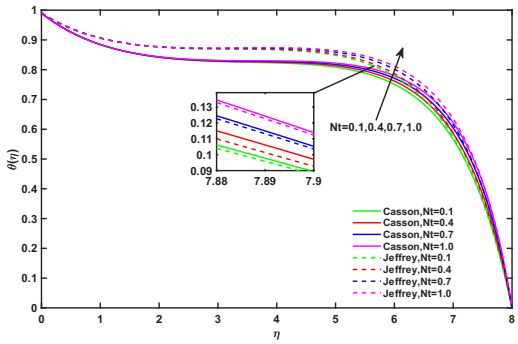

Figure 9: Velocity profile for $0.3 \leq K_1 \leq 0.9$

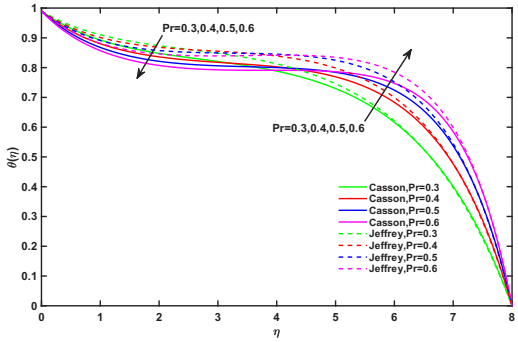

Figure 10: Velocity profile for $0.3 \leq K_1 \leq 0.9$

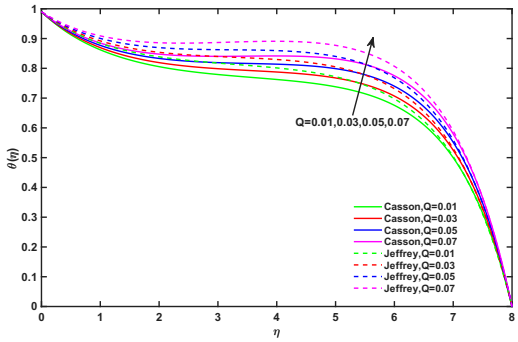

Figure 11: Velocity profile for $0.3 \leq K_1 \leq 0.9$

greater redistribution within the boundary layer and consequently reducing the concentration near the surface. Higher thermophoresis parameters (Nt) increase the thermophoretic force, which causes more nanoparticles to move from the heated wall into the fluid, thus increasing the concentration profile, as can see in Figure 17. Figure 18 displays that increasing Kr strengthens the consumptive reaction, which removes nanoparticles from the liquid more rapidly. This increased reaction reduces the overall concentration. In Figure 19, As the solute stratification parameter increases, the surrounding solute concentration increases, weakening the concentration gradient at the wall. Therefore, the concentration decreases more rapidly.

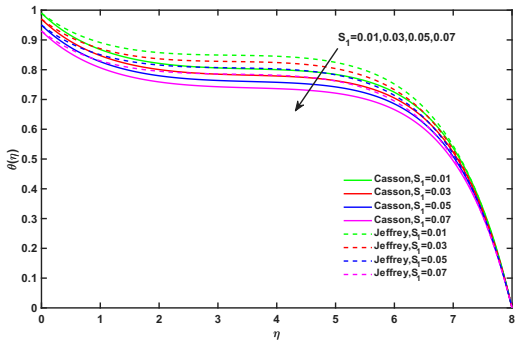

Figure 12: Velocity profile for $0.3 \leq K_1 \leq 0.9$

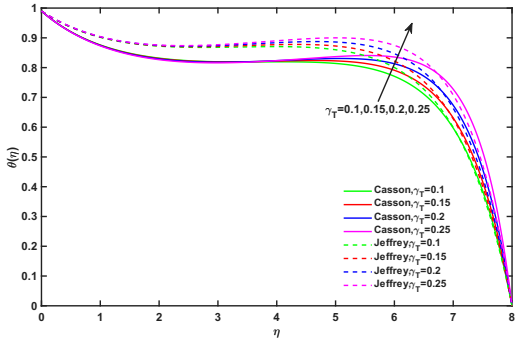

Figure 13: Velocity profile for $0.3 \leq K_1 \leq 0.9$

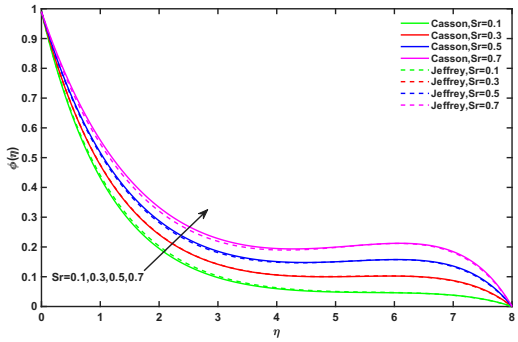

Figure 14: Concentration profile for $0.1 \leq Sr \leq 0.7$

In Figure 20, Skin friction rate increases with increasing Hartmann number and Grashoff number Casson fluid shows slightly higher skin friction than Jeffrey fluid. Figure 21 shows that the skin-friction rate decreases because increasing the porosity and suction parameters weakens the velocity profile near the wall, reducing the velocity slope at the surface. The reduced motion gradient directly reduces the shear stress on the wall. Figure 22 explains that the Nusselt number increases with both Pr and Nr. Higher Prandtl number reduces thermal diffusivity, increasing the wall temperature gradient, while increasing radiation parameter increases radiative heat transfer. Casson fluid consistently has a higher Nusselt number than Jeffrey fluid because its yield-stress behaviour produces a stronger

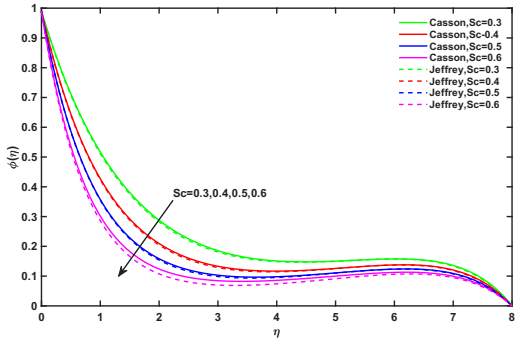

Figure 15: Concentration profile for $0.3 \leq Sc \leq 0.6$

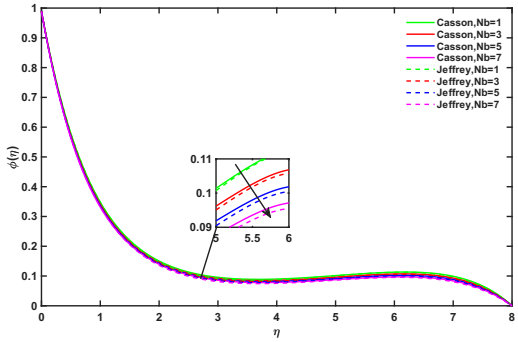

Figure 16: Concentration profile for$1 \leq Nb \leq 7$

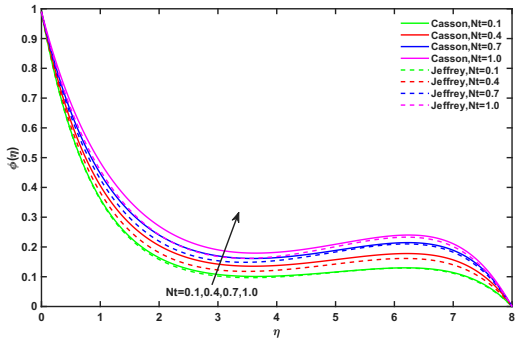

Figure 17: Concentration profile for $0.1 \leq Nt \leq 1.0$

heat-transfer rate. Figure 23 shows that the Nusselt number declines with Q and Du, as both reduce the wall thermal gradient, thereby reducing heat transfer. Figure 24 shows that the Nusselt number declines with increasing Nb and Nt, and the Casson fluid consistently exhibits a higher heat-transfer rate than the Jeffrey fluid. In fig.25, for both Casson and Jeffery fluids, the Sherwood number appears to increase with increasing Nb and its decreases with Nt. Fig.26 explains that Sherwood number rises with Kr because stronger reactions increase the consumption of species and widen the concentration gradient. However, it decreases with the Soret parameter (Sr) because stronger thermos diffusion reduces the concentration difference adjacent the wall, thereby dropping mass transmission. In fig-

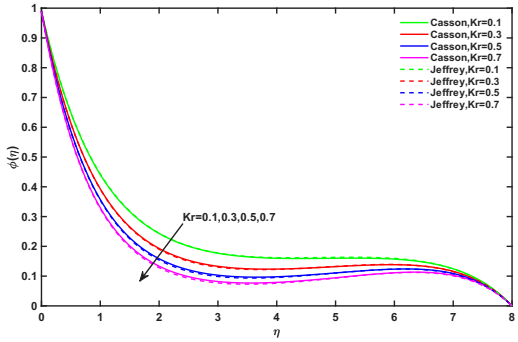

Figure 18: Concentration profile for $0.1 \leq Kr \leq 0.7$

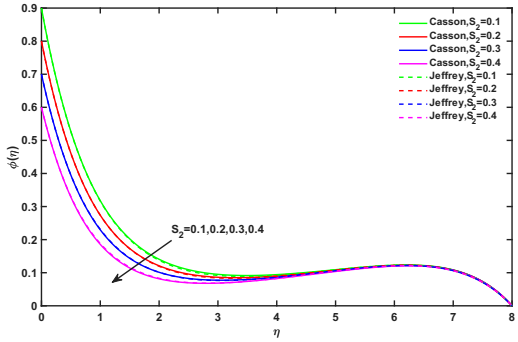

Figure 19: Concentration profile for $0.1 \leq S_2 \leq 0.4$

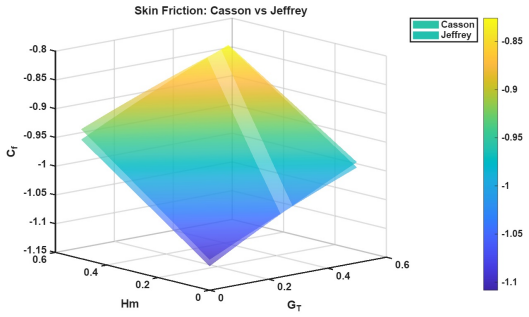

Figure 20: Skin friction coefficient for$Hm\&G_T$

ure 27 increasing both the Schmidt number and the mass relaxation coefficient increase the Sherwood number. Jeffrey fluid consistently shows slightly higher Sherwood numbers than Casson fluid due to lower flow resistance. Table 2-4 represent the numerical values of skin friction, Nusselt number and Sherwood number with various values for Casson and Jeffrey fluids.

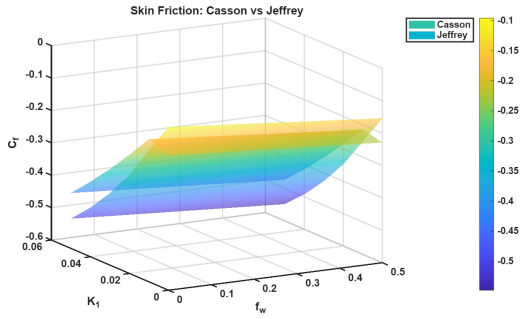

Figure 21: Skin friction coefficient for $K_1\&f_w$

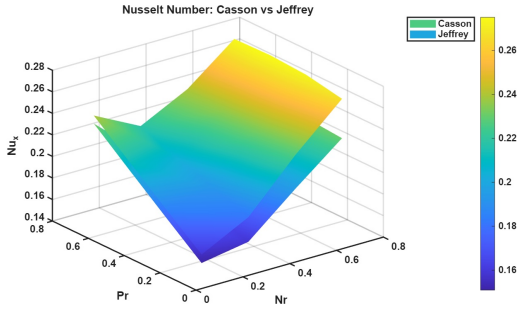

Figure 22: Nusselt number for Pr and Nr

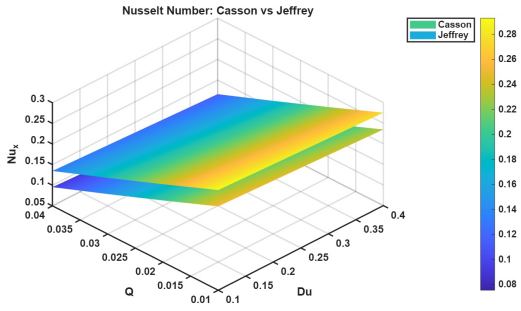

Figure 23: Nusselt number for Q and Du

Conclusion

This numerical analysis focuses on the comparative analysis of Casson-Jeffrey fluid on heat and mass transfer in MHD radiative flow on a Riga Plate, considering chemical reactions, free convection, cross-diffusion, thermal-mass stratification, thermophoresis, and Brownian motion. The bvp4c solver has also been used in the solution process. And verified the results for certain instances were discovered that the latest findings favorably align with the previous ones. The results of this study are concise below.

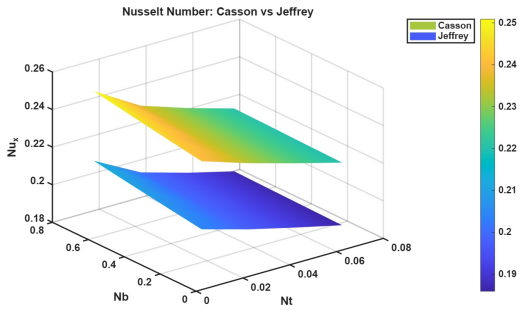

Figure 24: Nusselt number for $Nb\&Nt$

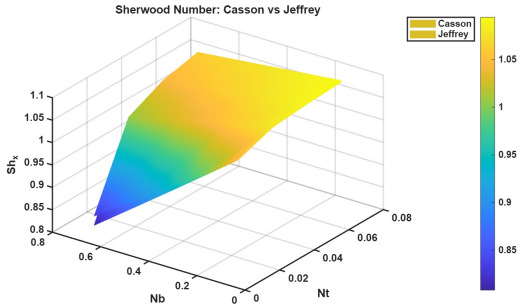

Figure 25: Sherwood number for $Nb\&Nt$

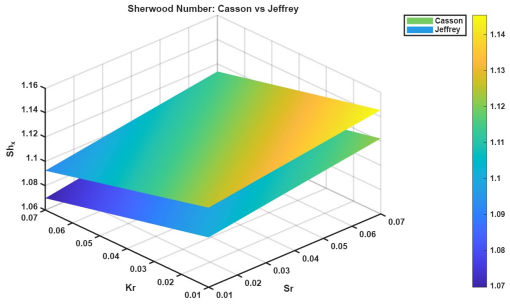

Figure 26: Sherwood number for$Kr\&Sr$

- For Casson and Jeffrey fluids, the velocity profile declines with growing values of the porosity parameter, while increases with the Grashof number and Hartmann number.
- The temperature profile intensifies sharply with increasing Dufour number, thermophoresis, and Brownian motion parameters, whereas it declines decisively under stronger thermal stratification.
- At high Schmidt number and chemical reactivity, the concentration outline diminishes sharply, while an increase in Soret number broadens the concentration distri-

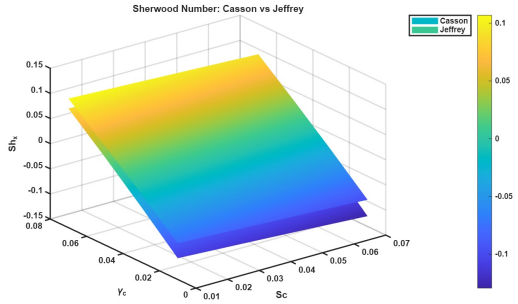

Figure 27: Sherwood number for $Sc\&\gamma_C$

Table 2: Numerical values of skin friction coefficient with for some parameters when $\boldsymbol{Nr} = 0.2$, $\boldsymbol{Pr} = 0.5$, $\boldsymbol{S}_1 = 0.01, \boldsymbol{S}_2 = 0.01$, $\boldsymbol{Du} = 0.2, \boldsymbol{Sr} = 0.5, \boldsymbol{Nb} = 1, \boldsymbol{Nt} = 0.1$, $\boldsymbol{Q} = 0.05$, $\boldsymbol{\delta} = 0.01$, $\boldsymbol{Kr} = \boldsymbol{Sc} = 0.5$, $\boldsymbol{\gamma_T} = \boldsymbol{\gamma_C} = 0.01$. for Casson and Jeffrey fluids.

G_T	Hm	K_1	f_w	**Casson fluid** $\frac{C_{f_x} Re_x^{1/2}}{2}$	**Jeffrey fluid** $\frac{C_{f_x} Re_x^{1/2}}{2}$
0.1	0.1	0.3	1	−0.521369370	−0.453121093
0.5				−0.469723786	−0.382107539
0.9				−0.430735211	−0.333761992
1.3				−0.400370942	−0.299102374
0.1	0.1			−0.521369370	−0.453121093
	0.5			−0.305468729	−0.258122064
	0.9			−0.093732568	−0.069087693
	1.3			0.114122126	0.114608838
		0.3		−0.521369370	−0.453121093
		0.5		−0.697897274	−0.588895499
		0.7		−0.849973912	−0.705242814
		0.9		−0.983854490	−0.807338600
			1.0	−0.521369370	−0.453121093
			1.3	−0.533919371	−0.464922712
			1.5	−0.539636650	−0.470282751
			1.7	−0.544056790	−0.474414027

bution considerably.

- The skin-friction rate rises as the Hartmann and Grashoff numbers increase, but it falls with higher porosity and suction parameters. In addition, the Casson fluid exhibits slightly greater skin friction than the Jeffrey fluid.
- The Nusselt number grows with rising Prandtl number and radiation parameter, yet it drops as the heat source and Dufour number intensify.
- The Sherwood number surges with increasing Brownian motion, yet it declines as the Soret number rises.
- The Jeffrey fluid shows lower velocity than the Casson fluid because its viscoelastic relaxation and retardation effects increase flow resistance, slowing the fluid near the surface. Consequently, its slower motion weakens convective heat transport, causing heat to accumulate and the temperature profile to rise compared to the faster-flowing Casson fluid. but concentration is dominated by diffusion, making the profiles almost the same.

Future scope

Future work can extend the study to time-dependent flow, different non-Newtonian

Table 3: Numerical values of Nusselt number with for some parameters when $Hm = 0.1$, $f_w = 1$, $G_T = 0.1$, $S_1 = 0.01$, $S_2 = 0.01$, $Sr = 0.5$, $\delta = 0.01$, $Kr = Sc = 0.5$, $\gamma_T = \gamma_C = 0.01$, $K_1 = 0.3$. for Casson and Jeffrey fluids.

Pr	Nr	Q	Du	Nb	Nt	**Casson fluid** $Nu_x Re_x^{-1/2}$	**Jeffrey fluid** $Nu_x Re_x^{-1/2}$
0.3	0.2	0.05	0.2	1	0.1	0.317946119	0.281679563
0.4						0.371575549	0.325176852
0.5						0.423449583	0.369887311
0.6						0.474779217	0.414075427
0.5	0.2					0.391666086	0.342040086
	0.4					0.413886745	0.360796566
	0.6					0.434525610	0.378897851
	0.8					0.454322984	0.396885218
		0.01				0.416811302	0.370126559
		0.03				0.404394058	0.356297061
		0.05				0.391666086	0.342040086
		0.07				0.378605571	0.327319257
			0.2			0.333693874	0.283671485
			0.4			0.274801411	0.224348021
			0.6			0.222149712	0.171285431
			0.8			0.176265368	0.125016959
				1		0.348376205	0.305052506
				3		0.263761942	0.232842371
				5		0.204054225	0.181876100
				7		0.161734282	0.145604152
					0.1	0.348376205	0.305052506
					0.4	0.347442339	0.304345270
					0.7	0.346457919	0.303590865
					1.0	0.345424979	0.302790771

nanofluids, variable thermal properties, nonlinear radiation, porous media, and entropy generation. ANN and optimization techniques can also be used to predict and enhance heat and mass transfer performance in advanced thermal and industrial applications.

Table 4: Numerical values of Sherwood number with for some parameters when $Hm = 0.1$, $f_w = 1$, $G_T = 0.1$, $Nr = 0.2$, $Pr = 0.5$, $S_1 = 0.01$, $S_2 = 0.01$, $Du = 0.2$, $Q = 0.05$, $\delta = 0.01$, $\gamma_T = 0.01$, $K_1 = 0.3$. for Casson and Jeffrey fluids.

Sr	Kr	Sc	γ_C	Nb	Nt	**Casson fluid** $Sh_x Re_x^{-1/2}$	**Jeffrey fluid** $Sh_x Re_x^{-1/2}$
0.1	0.5	0.5	0.01	1	0.1	0.920484482	0.901790430
0.3						0.857170980	0.846076852
0.5						0.793716733	0.790268876
0.7						0.730121052	0.734366099
	0.1					0.632274778	0.621158259
	0.3					0.719335210	0.713210045
	0.5					0.793716733	0.790268876
	0.7					0.859756063	0.857939001
		0.3				0.523131611	0.526572526
		0.4				0.667334206	0.666716177
		0.5				0.793716733	0.790268876
		0.6				0.907438369	0.901879612
			0.01			0.838790227	0.832069729
			0.03			0.938218173	0.924969918
			0.05			1.035780227	1.017507226
			0.07			1.115780227	1.109241945
				1		0.796284654	0.792421175
				3		0.846688853	0.836491329
				5		0.871245001	0.857975867
				7		0.887406176	0.872212213
					0.1	0.796284654	0.792421175
					0.4	0.712731159	0.719141074
					0.7	0.630697911	0.647389302
					1.0	0.550199776	0.577175257

Nomenclature

u	x-Axis Velocity $(\mathrm{m\,s^{-1}})$
U_w	stretching sheet velocity $(\mathrm{m\,s^{-1}})$
v	y-Axis Velocity $(\mathrm{m\,s^{-1}})$

v_w	suction velocity ($\mathrm{m\,s^{-1}}$)
T	Fluid Temperature (°C)
T_w	Solid Wall Temperature
T_∞	Free Stream Temperature
C_p	Specific Heat at Constant Pressure ($\mathrm{J\,K^{-1}\,kg^{-1}}$)
B_0	Magnetic Field Strength ($\mathrm{A\,m^{-1}}$)
ρ	Density ($\mathrm{kg\,m^{-3}}$)
v	Kinematic Viscosity ($\mathrm{m^2\,s^{-1}}$)
μ	Dynamic Viscosity ($\mathrm{kg\,m^{-1}\,s^{-1}}$)
g	Gravitational Acceleration ($\mathrm{m\,s^{-2}}$)
D_m	diffusivity
Q	Heat source
G_r	Grashof number
θ	non-Dimensional Temperature
Ec	Eckert number
Kr	Homogenous reaction
Nb	Brownian motion
Nu_x	Nusselt Number
τ_w	Surface Shear Stress
q_w	Heat Transfer Rate
Re_x	Reynolds Number
C_{f_x}	Skin Friction Coefficient
δ	velocity slip parameter
f_w	Suction/injection parameter
Nt	Thermophoresis parameter
Fr	Darcy–Forchheimer parameter
Sc	Schmidt number
λ	Stretching/Shrinking parameter
Hm	Modified Hartmann number
β_1	Magnitude of electrodes
β	Casson fluid parameter
K	Jeffrey fluid parameter
Hm	Hartmann number
K_1	porous media
Pr	Prandtl number

γ_T, γ_c	thermal, and solute relaxation
S_1, S_2	thermal and mass stratification parameter
K	Porosity factor
q_r	flux of radiant heat
Pr	Prandtl Number
Nr	Radiation parameter
$f'(\eta)$	non-Dimensional velocity
ϕ	non-Dimensional Concentration

References

[1] H Alrihieli. Thermal-hydrodynamic analysis of a maxwell fluid with controlled heat/mass transfer over a riga plate: A numerical study with engineering applications. *Results in Engineering*, 26:104801, 2025.

[2] F A Alwawi and E A El-Sayed. Computational and regression analysis of emhd casson tri-hybrid nanofluid flow over a radiant riga plate: Viscous dissipation, suction, and shape factor considerations. *Advances in Mechanical Engineering*, 17(8):16878132251370790, 2025.

[3] A Ali, M N Aslam, and M S Junaid. A comparative analysis of darcy–forchheimer nanofluid flow with thermal and solutal effects over a riga plate. *Journal of Thermal Analysis and Calorimetry*, 150:1887–1905, 2025.

[4] H Alhazmi. Applications of thermal radiation on non-newtonian fluid flow subject to cattaneo-christov heat/mass flux and double stratifications over a riga plate. *Journal of Radiation Research and Applied Sciences*, 18(3):101751, 2025.

[5] M Z Ahmed, V Dhanalaxmi, and S Panda. Thermal analysis on ferro casson nanofluid flow over a riga plate with thermal radiation and non-uniform heat source/sink. *Modern Physics Letters B*, 39(11):2450460, 2025.

[6] O Adebisi. Investigation of heat transfer in a radiative casson triple particle nanofluid flow with riga plate and variable thermo-physical characteristics. *Nano-Structures & Nano-Objects*, 42:101486, 2025.

[7] A Ali. Thermal stratification of darcy-forchheimer nano-fluid flow with cattaneo-christov heat flux over a riga plate: A mathematical analysis. *Case Studies in Thermal Engineering*, page 106794, 2025.

[8] K Bhaskar, K Sharma, and K Bhaskar. Steady flow of jeffery–hamel casson hybrid nanofluid for thermal enhancement with impacts of soret–dufour. *Physics of Fluids*, 37(9), 2025.

[9] M Bhaskar, K R Babu, and S U Khan. Multiscale modeling of jeffrey-casson immiscible fluid dynamics under electrokinetic and magnetohydrodynamic effects. *Multiscale and Multidisciplinary Modeling, Experiments and Design*, 8:383, 2025.

[10] H Basha. Influence of variable fluid properties on mhd three-dimensional (3d) maxwell nano-liquid flow over convectively heated stretchable riga plate with thermal radiation and soret-dufour phenomena. *Journal of Nanofluids*, 14(1):81–94, 2025.

[11] S Choudhary, A Mehta, and R Mehta. Computational analysis of thermophoresis and brownian motion effects in bioconvective mhd casson hybrid nanofluid (ag-al2o3/h2o) flow past a moving slender needle. *Results in Engineering*, page 106947, 2025.

[12] S Choudhary, R Mehta, and T Mehta. Numerical study of mhd williamson hybrid nanofluid flow over incessantly moving thin needle in presence of soret & dufour effect. *Partial Differential Equations in Applied Mathematics*, page 101294, 2025.

[13] S Choudhary. Numerical analysis on mhd heat transfer of casson hybrid nanofluid (cu-al2o3/h2o) flow across an inclined moving plate in presence of radiation. *Canadian Journal of Physics*, 103(9):846–859, 2025.

[14] S Eswaramoorthi, K Loganathan, and P Choudhary. Computational analysis of sutterby nanofluid with heat and mass convective conditions: a comparative study of riga plate and stationary plate. *Discover Applied Sciences*, 7:159, 2025.

[15] A M Galal. Optimizing thermal and solutal dynamics trihybrid nanofluid fluid flow in industrial processes: The potential of thermal radiation and chemical reaction. *Journal of Radiation Research and Applied Sciences*, 18(2):101413, 2025.

[16] Govind. Numerical investigation of thermal and mass diffusion characteristics in chemically reactive and magnetite cu–al2o3 water-based hybrid nanofluid flow over riga plate. *Advanced Theory and Simulations*, 8(10):e00352, 2025.

[17] R Mehmood, Noreena, and S Rana. Thermally stratified electrically conducting flow interacting mwcnt/swcnt hybrid nanofluid over an inclined riga plate with variable viscosity and thermal slip: application in nanotechnology. *Journal of Thermal Analysis and Calorimetry*, 150:3751–3765, 2025.

[18] R Mehta and K Senthilvadivu. Artificial neural network analysis on heat and mass transfer in mhd carreau ternary hybrid nanofluid flow across a vertical cylinder: A numerical computation. *International Journal of Thermofluids*, 27:101171, 2025.

[19] K Muhammad. Significance of brownian diffusion and thermophoresis in energy and mass optimization for newtonian and non-newtonian fluid flow: A numerical study via keller-box method. *Case Studies in Thermal Engineering*, 72:106365, 2025.

[20] S M Sachhin, U S Mahabaleshwar, and S W Joo. Irreversible mechanism and thermodynamics impact on chemically reactive maxwell hybrid nanofluid flow with thermophoresis and brownian motion: Nanotechnology applications. *Arabian Journal for Science and Engineering*, 2025.

[21] H F Shankar and M Kulkarni. Double diffusive mixed convective flow over a wedge and cone in the presence of brownian diffusion and thermophoresis parameter. *Numerical Heat Transfer, Part A: Applications*, 86(18):6336–6348, 2025.

[22] D Thenmozhi. Dynamics of heat transfer in complex fluid systems: Comparative analysis of jeffrey, williamson and maxwell fluids with chemical reactions and mixed

convection. *International Journal of Thermofluids*, 24:100896, 2024.

[23] S Varshegaa, E Ragulkumar, and F Peter. Thermal and mass transfer performance of non-newtonian fluids under mhd and chemical reaction effects with thermophoresis and brownian motion. *Discover Applied Sciences*, 7:748, 2025.

[24] H Yasmin. Novel physical applications of thermal radiation within the dissipative emhd casson fluid flow past a horizontal riga plate. *Journal of Radiation Research and Applied Sciences*, 18(2):101335, 2025.

[25] R M Kumar, R S Raju, F Mebarek-Oudina, M A Kumar, and V K Narla. Cross-diffusion effects on an mhd williamson nanofluid flow past a nonlinear stretching sheet immersed in a permeable medium. *Frontiers in Heat and Mass Transfer*, 22(1):15–34, 2024.

[26] G Ramasekhar, F Mebarek-Oudina, S Suneetha, H Vaidya, and P D Selvi. Computational simulation of casson hybrid nanofluid flow with rosseland approximation and uneven heat source/sink. *International Journal of Thermofluids*, 24:100893, 2024.

[27] D Iranian, F Mebarek-Oudina, S Karthik, H Fish, and M Helal. Bioconvective casson fluid flow over a slender needle under magnetic dipole influence: Coupled thermal and chemical transport analysis. *Case Studies in Thermal Engineering*, page 107722, 2026.